Original Article

Institution of MECHANICAL ENGINEERS

Journal of MECHANICAL ENGINEERING SCIENCE

Proc IMechE Part C:
J Mechanical Engineering Science
0(0) 1–15

DOI: 10.1177/0954406220978437
journals.sagepub.com/home/pic

SAGE

Kinematics analysis and performance testing of 6-RR-RP-RR parallel platform with offset RR-hinges based on Denavit-Hartenberg parameter method

Yang Zhang[1,2], Ha-si-ao-qi-er Han[1], Zhen-bang Xu[1,2], Chun-yang Han[1,2], Yang Yu[1], A-long Mao[1] and Qing-wen Wu[1]

Abstract

A six degrees-of-freedom parallel platform in a 6-RR-RP-RR configuration with high accuracy, high stiffness and a large working stroke is studied for application to the sub-mirror adjustment system of a large-aperture telescope. To meet the performance requirements, the parallel platform adopts a self-centering and well-designed offset universal hinge. The two hinge axes of the offset hinge do not intersect but have a specific offset in space, which makes the kinematics more complex than that with a common universal hinge. Therefore, to solve this complex kinematics problem, this paper innovatively introduces the Denavit–Hartenberg (D-H) parameter method that is used for series mechanisms. The method has a simple modeling process, strong applicability and continuity, providing a new tool for the analysis and application of the parallel mechanisms. A kinematics model of the parallel platform can be constructed and solved using a numerical iteration method. The accuracy of the numerical kinematics solution is verified using a co-simulation method. This paper analyses the passive derivative motion and the leg length error is compensated. Finally, test studies of the motion resolution, the repetitive positioning accuracy, the motion stroke, the static stiffness of the legs, and the static stiffness and dynamic stiffness of the entire machine were also carried out to verify the platform's performance.

Keywords

Parallel platform, RR-RP-RR kinematic chain, offset hinge, kinematics, D-H parameter method

Date received: 24 January 2020; accepted: 21 August 2020

Introduction

Since the parallel mechanism was first devised, it has been widely used in many fields because of its high overall rigidity, high bearing capacity and high precision, including motion simulators,[1] micro vibration simulator,[2] telescope secondary mirror adjustment mechanisms,[3] force or torque sensors,[4] parallel machine tools.[5–8] In addition, parallel mechanisms are also used in medical applications,[9] such as spherical parallel mechanism for robotic-assisted craniotomy,[10] a novel 3UPS/RPU parallel kinematic mechanism as a knee rehabilitation and diagnosis mechatronics system,[11] minimally invasive surgery systems,[12] and parallel robots used to assist in eye surgery.[13]

In recent years, the theoretical research into parallel mechanism has seen rapid development, especially in kinematics analysis. Harib et al.[14] considered the arrangements of the universal hinges and the friction effect in their study of the kinematics of the 6-UPS parallel manipulator. Kim et al.[15] studied the inverse kinematics and inverse dynamics of a 6-PUS parallel mechanism. Song et al.[16] used the screw theory to perform kinematic analysis and optimization design on a new type of five-degree-of-freedom parallel robot, and established a motion and force mapping model. Sun et al.[17] proposed a generalized method for

[1]Changchun Institute of Optics, Fine Mechanics and Physics, Chinese Academy of Sciences, Changchun, China
[2]Center of Materials Science and Optoelectronics Engineering, University of Chinese Academy of Sciences, Beijing, China

Corresponding authors:
Ha-si-ao-qi-er Han, Changchun Institute of Optics, Fine Mechanics and Physics, Chinese Academy of Sciences, No.3888, Dong Nanhu Road, Changchun 130033, China.
Email: hanhasiaoqier@yahoo.com
Zhen-bang Xu, Changchun Institute of Optics, Fine Mechanics and Physics, Chinese Academy of Sciences, No.3888, Dong Nanhu Road, Changchun 130033, China.
Email: xuzhenbang@ciomp.ac.cn

analyzing the inverse kinematics of PMs using the finite screw theory, and this method has high accuracy. Gan et al.[18] studied the forward kinematics of a new type of parallel mechanism denoted by 1CCC-5SPS, in which the cylindrical joints are stiffer than traditional spherical joints, using Gröbner's basis theory. Liu et al.[19] analyzed the inverse kinematics of a hydraulically driven 6-UCU parallel platform. Traditional universal hinges present some problems, including low stiffness and limited working space. Therefore, researchers have designed different types of hinges to replace traditional universal hinges and spherical hinges. Groβmann et al.[20] discussed three possible types of eccentric universal hinges from the perspective of the shortcomings of traditional universal hinges. Eccentric universal hinges have larger rotation spaces and offer higher stiffness, but they also make the motion transformation more complex. Gloess et al.[21] designed an offset universal joint with stiffness of up to twice that of a conventional universal joint to meet the high stiffness and high load requirements of parallel platforms. The designs of this type of hinge require fewer components and can be manufactured more accurately. Ji et al.[22] studied the kinematics of a 3-UPU parallel manipulator with offset hinges. The mechanism was found to have rotational singularities. Hu et al.[23] analyzed the kinematics and the workspace of an offset 3-RRPRR parallel manipulator. The 3-RRPRR configuration with offset hinge has a larger reachable workspace than its similar structure 3-RRPU, 3-RPRU, 3-UPU. Dalvand et al.[24,25] studied a 6-RRCRR parallel platform with offset universal hinges and proposed a numerical solution to resolve the platform's kinematics problems. Han et al.[26] studied the inverse kinematics of a novel 6-P-RR-R-RR parallel platform. The slider displacement was obtained directly by establishing an iterative formula for the slider displacement and the two hinge variables. But the hinge motion constraint method mentioned above can only solve the leg length or slider displacement, which cannot solve the velocity relationship, acceleration relationship, working space and singularity. It has no continuity and has great limitations.

The offset universal hinge mentioned above is also known as an RR offset hinge. To meet the mechanism's high precision, high stiffness and large working stroke requirements, a 6-RR-RP-RR parallel platform with an RR offset hinge is proposed in this paper. The offset hinge is easier to manufacture with fewer geometric constraints, the limit rotation angle is larger, and the components are more compact, increasing the stiffness and precision of the hinge and the parallel mechanism. But the introduction of the offset variable of the hinge axis makes the kinematics solution more complex than that of the parallel mechanism using the universal hinge. And it is difficult to solve effectively, and there is no analytical solution. Moreover, the existing methods[24–26] have great limitations. Therefore, this paper innovatively proposes a Denavit–Hartenberg (D-H) parameter method based on a series mechanism[27,28] to provide an effective solution to the kinematics problems of the parallel platform. It overcomes the shortcomings of the complex modeling process, large limitations and the poor continuity of the hinge motion constraint method, has strong operability and adaptability, and can be extended to the kinematics analysis of various parallel mechanisms. It has very good application value for the kinematic analysis of the parallel mechanism. It can solve the variables at all joints of each leg chain, and lays the foundation for the subsequent dynamic analysis. Each leg actuator is regarded as a series mechanism composed of six joints and a kinematics model is established for each leg. The kinematics model of the parallel platform for the entire machine is then constructed and solved using a numerical iterative method. The derivative motion introduced by the actuated ball screw pair (RP) is also analyzed.

The remainder of this article is as follows. The next section presents the composition of the complete platform, the leg actuator design and the offset hinge design. Then, the parallel platform configuration parameters and the kinematic chain, along with its D-H parameters are described. In 'Kinematic analysis of the platform' section, the kinematics of the entire platform are studied. In 'Inverse solution for speed and acceleration' section, the velocity and the acceleration are derived. In the penultimate section, the performance parameters are tested and studied. The final section summarizes the results for the paper.

Design of prototype

A 6-RR-RP-RR adjusting mechanism (composed of a combination of offset hinges and ball screw pairs) is used in this paper. The two axes of the RR hinge are offset rather than intersecting. With regard to the accuracy of the whole platform, the accuracy of the leg actuator has a direct impact on the overall accuracy. In addition, the clearance and the internal friction of the offset hinges will also affect the platform accuracy. Furthermore, the design of the hinges will play an important role in determining the stiffness of the platform. Therefore, the design of the platform largely refers to the designs of the leg actuator and the hinge.

Overall structure of the platform

The configuration and the structural components of the parallel platform are shown in Figure 1. The platform is mainly composed of six leg actuators, in accordance with the designed configuration. Each leg actuator is connected to both the mobile and base platforms via offset hinges. The number of

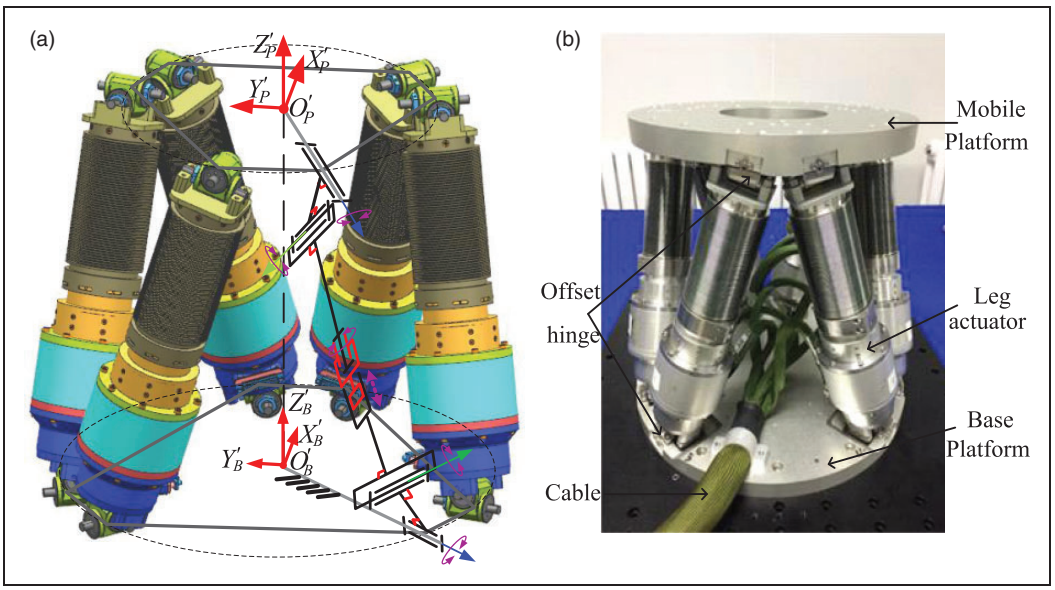

Figure 1. Configuration and structural components of the parallel platform: (a)The diagram of the mechanism, (b) the prototype.

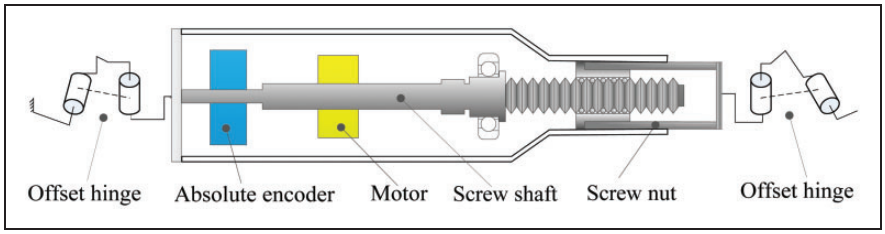

Figure 2. Structure of leg actuator.

DOFs of the parallel platform can be calculated using the Kutzbach-Grübuler formula, as follows:

$$F = 6(n - g - 1) + \sum_{i=1}^{g} f_i \tag{1}$$

In the formula, n is the total number of components; g is the total number of kinematic pairs; and f_i is DOFs of i_{th} kinematic pair.

It can be seen from Figure 1 that n is 14 and g is 18, including 12 offset hinges with two rotational DOFs and six ball screw pairs with two rotational DOFs. Upon substitution of these values into formula, the parallel platform has six degrees of freedom.

Design of the leg actuator

The structure of the leg actuator is shown in Figure 2. The overall intention is to drive the precision ball screw using the motor. To ensure high-precision control, a 17-bit absolute encoder is used to provide feedback, and is connected directly to the screw. The upper and lower platforms are connected to the leg actuator via offset hinges to achieve high stiffness.

Design of the offset hinge

The hinge stiffness represents an important part in the platform stiffness. The hinge design should consider both the load and the clearance comprehensively according to the design requirements.

Figure 3 shows the internal structure of the designed offset hinge. The offset hinge consists of hinge shafts, shell, nut, end cap, steel ball, and silicone rubber seal ring. Limitation of the platform in the Z direction with a large stroke and a small envelope size requires the hinge to have a small offset and high rigidity. The offset variable of the hinge is U_{offs}, and a dense bead shaft system is adopted so that the steel balls on both sides of each hinge shaft are in a full circle and are symmetrically arranged to replace the diagonal contact ball bearings. Quantitative preloading through nuts and end caps can greatly reduce the axial clearance, thereby enhancing the hinge stiffness. Additionally, the overall structure is compact, which reduces the size while also greatly reducing the offset variables. Hinge mounting bases are arranged on one side of each hinge shaft to improve hinge accuracy. Silicone rubber seal ring is used to seal the grease used for steel ball.

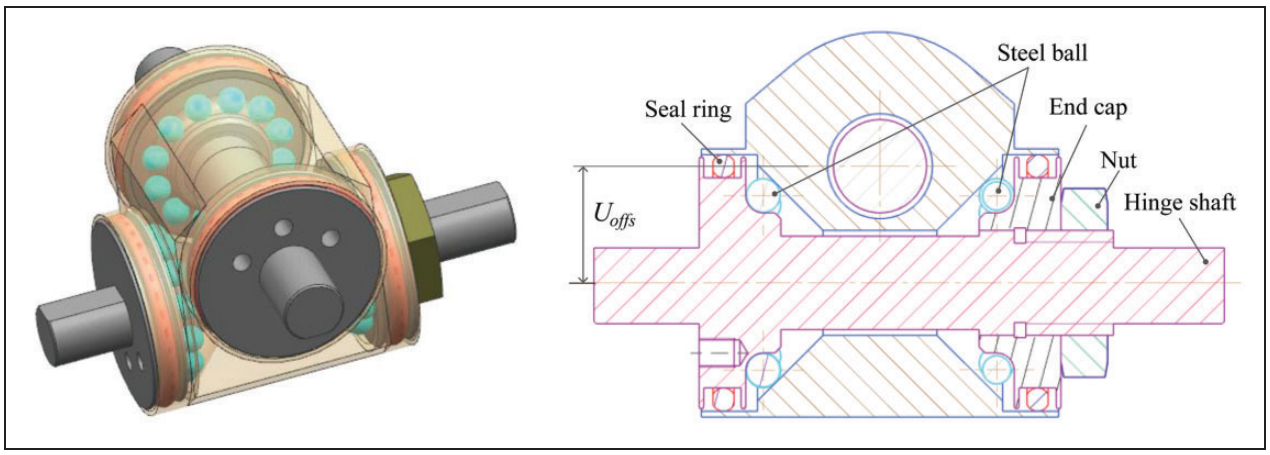

Figure 3. Internal structure of the offset hinge.

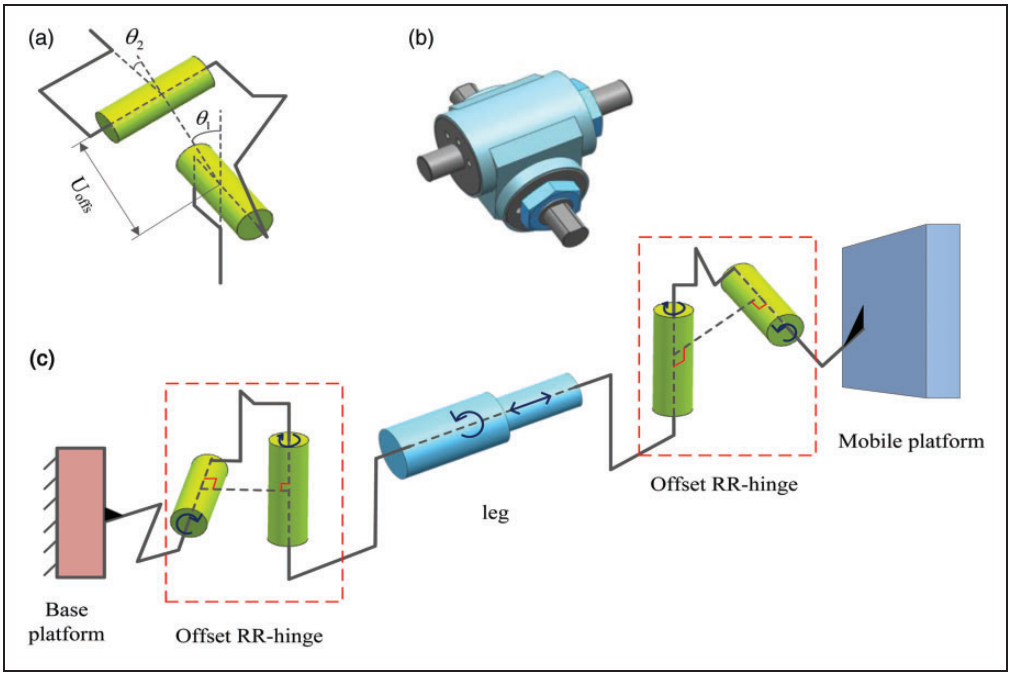

Figure 4. RR-RP-RR kinematic chain: (a) Schematic of the offset RR-hinge, (b) 3D model of the offset RR-hinge, and (c) the RR-RP-RR kinematic chain.

Kinematic chain

Description of the architecture

As shown in Figure 1, the moving platform is connected to the static platform through the hinges and the legs, which are driven using ball screw pairs. Figure 4 illustrates offset RR hinges and the RR-RP-RR composition used for the leg-driving chain of the parallel platform.

Because of the presence of the offset RR hinge, it is difficult to solve the kinematics problems using conventional kinematics solution methods. To analyze the kinematics of the 6-RR-RP-RR parallel platform, the D-H parameter method for a series mechanism is introduced to establish a kinematics model of a single leg. Figure 5 shows the kinematic chain of the i_{th} leg.

To describe the motion of the upper platform (i.e., the mobile platform), the global coordinate system $O_B - X_B Y_B Z_B$ is established at the center O_B of the lower surface of the base platform. The body frame $O_P - X_P Y_P Z_P$ is then established at the center O_P of the upper surface of the moving platform. The hinge points P_i and B_i $(i = 1, \ldots, 6)$ are shown in Figure 6. The offset variables of the upper and lower offset hinges are expressed as U_{p_offs} and U_{b_offs}, respectively. The parallel platform's configuration parameters are given in Table 1.

The spatial pose of the upper platform in the $O_B - X_B Y_B Z_B$ system is determined using the vector $[X, Y, Z, \alpha, \beta, \gamma]$. According to the RPY rules, the

transfer matrix ${}^{O_B}T_{O_P}$ can be expressed as:

$$ {}^{O_B}T_{O_P} = \begin{bmatrix} c\beta c\gamma & -c\beta s\gamma & s\beta & X \\ c\alpha s\gamma + s\alpha s\beta c\gamma & c\alpha c\gamma - s\alpha s\beta s\gamma & -s\alpha c\beta & Y \\ s\alpha s\gamma - c\alpha s\beta c\gamma & s\alpha c\gamma + c\alpha s\beta s\gamma & c\alpha c\beta & Z \\ 0 & 0 & 0 & 1 \end{bmatrix} \tag{2} $$

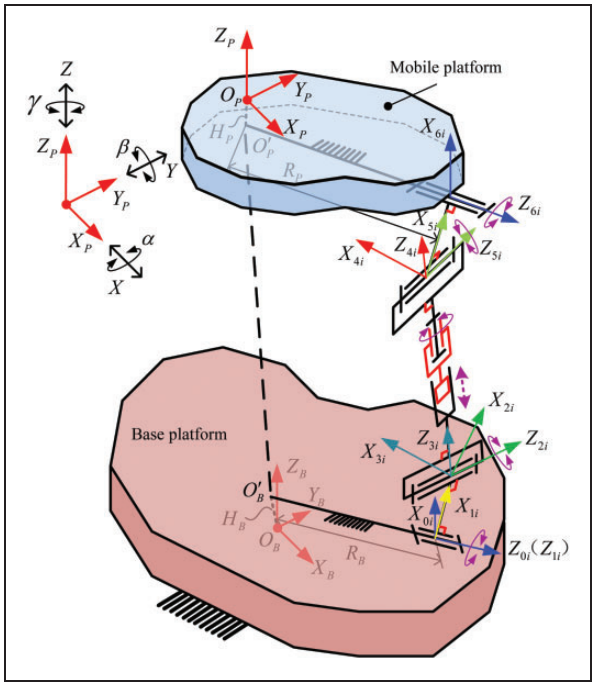

Figure 5. Definition of the coordinate system used for the i_{th} leg kinematic chain.

where s()=sin() and c()=cos(); the same notation applies to subsequent matrices.

D-H Parameters and kinematics of the i_{th} leg

As shown in Figure 5, seven local coordinate systems denoted by $O_{0i} - X_{0i}Y_{0i}Z_{0i}(i = 1, \ldots, 6)$ are established, where O_{0i} coincides with the lower hinge point B_i and O_{6i} coincides with the upper hinge point P_i. Each leg can be regarded as an RR-RP-RR series mechanism, and the D-H parameters of the i_{th} leg are given in Table 2.

The transformation matrix between two adjacent coordinate systems $O_n - X_nY_nZ_n$ and $O_{n+1} - X_{n+1}Y_{n+1}Z_{n+1}$ is:

$$ \begin{aligned} {}^{n}T_{n+1} &= A_{n+1} \\ &= Rot(x, \alpha_n) \times Trans(a_n, 0, 0) \times Rot(z, \theta_{n+1}) \\ &\quad \times Trans(0, 0, d_{n+1}) \end{aligned} \tag{3} $$

Table 2. D-H parameters of the i_{th} leg.

Link j	θ_{ji}(°)	d_{ji}(m)	$a_{(j-1)i}$(m)	$\alpha_{(j-1)i}$(°)
1	θ_{1i}	0	0	0
2	θ_{2i}	0	U_{b_offs}	90
3	θ_{3i}	0	0	−90
4	0	L_{4i}	0	0
5	θ_{5i}	0	0	90
6	θ_{6i}	0	U_{p_offs}	−90

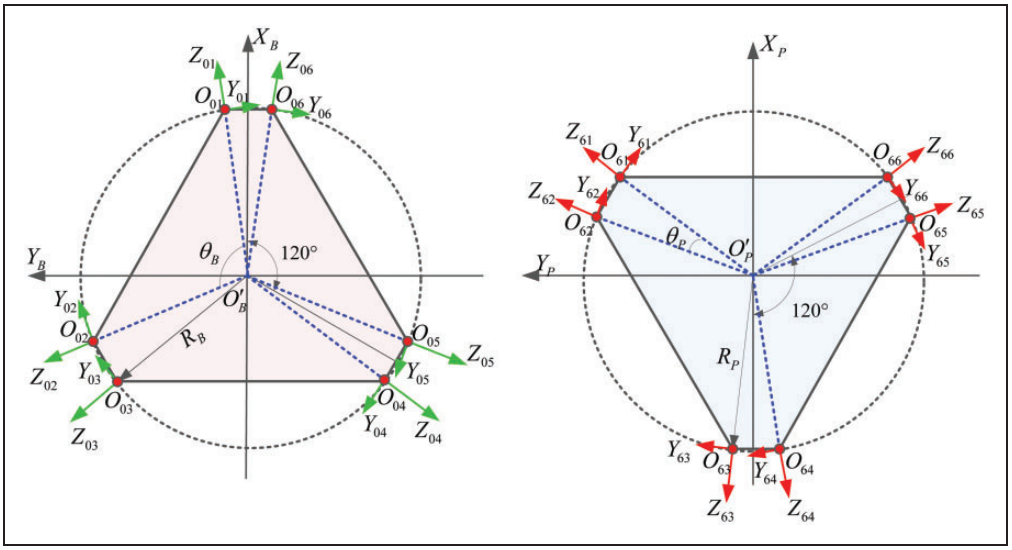

Figure 6. Local coordinate system at the hinge point.

Table 1. Configuration parameters of the parallel platform.

Parameter	R_P	R_B	θ_P	θ_B	U_{b_offs}	U_{p_offs}	H	H_P	H_B
Value	0.125 m	0.160 m	24°	96°	0.01 m	0.01 m	0.295 m	0.026 m	0.027 m

Kinematic analysis of the platform

Inverse kinematics

According to the D-H parameter method, the forward kinematics transformation matrix of the i_{th} leg of the kinematics chain can be derived to be:

$$ {}^{n}T_{6(i)} = A_{n+1(i)}A_{n+2(i)}\cdots A_{6(i)} \tag{4} $$

The position of O_{0i} in the $O_B - X_BY_BZ_B$ system is expressed as:

$$ {}^{O_B}O_{0_i} = [R_B \cdot c\theta_{O_{0i}} \quad R_B \cdot s\theta_{O_{0i}} \quad H_B]^T \tag{5} $$

In the above formula: $\theta_{O_{0i}} = \frac{\pi}{3}i - \frac{\theta_B}{2}$ $(i = 1, 3, 5)$, $\theta_{O_{0i}} = \frac{\pi}{3}(i-1) + \frac{\theta_B}{2}$ $(i = 2, 4, 6)$.

The transfer matrix ${}^{O_B}T_{O_{0i}}$ from the $O_{0i} - X_{0i}Y_{0i}Z_{0i}$ system (shown in Figures 5 and 6) to the $O_B - X_BY_BZ_B$ system is as follows:

$$ {}^{O_B}T_{O_{0i}} = \begin{bmatrix} {}^{O_B}R_{O_{0i}} & {}^{O_B}O_{0_i} \\ 0 & 1 \end{bmatrix} \tag{6} $$

In the above formula, after the $O_B - X_BY_BZ_B$ system rotates in the specific order 3-2, it has the same posture as the $O_{0i} - X_{0i}Y_{0i}Z_{0i}$ system.

$$ {}^{O_B}R_{O_{0i}} = \begin{bmatrix} c\theta_{Z_B(i)} & -s\theta_{Z_B(i)} & 0 \\ s\theta_{Z_B(i)} & c\theta_{Z_B(i)} & 0 \\ 0 & 0 & 1 \end{bmatrix} \bullet \begin{bmatrix} c\theta_{Y'_B(i)} & 0 & s\theta_{Y'_B(i)} \\ 0 & 1 & 0 \\ -s\theta_{Y'_B(i)} & 0 & c\theta_{Y'_B(i)} \end{bmatrix} \tag{7} $$

In the formula (7): $\theta_{Z_B(i)} = \frac{\pi}{3}(i+3) - \frac{\theta_B}{2}$ $(i = 1, 3, 5)$, $\theta_{Z_B(i)} = \frac{\pi}{3}(i-4) + \frac{\theta_B}{2}$ $(i = 2, 4, 6)$, $\theta_{Y'_B(i)} = -\frac{\pi}{2}$.

The position of O_{6i} in the $O_P - X_PY_PZ_P$ system is expressed as:

$$ {}^{O_P}T_{O_{6i}} = \begin{bmatrix} R_p \cdot c\theta_{O_{6i}} & R_p \cdot s\theta_{O_{6i}} & -H_p \end{bmatrix}^T \tag{8} $$

In the above formula: $\theta_{O_{6i}} = \frac{\pi}{3}i - \frac{\theta_P}{2}$ $(i = 1, 3, 5)$, $\theta_{O_{6i}} = \frac{\pi}{3}(i-1) + \frac{\theta_P}{2}$ $(i = 2, 4, 6)$.

The transfer matrix ${}^{O_P}T_{O_{6i}}$ from $O_{6i} - X_{6i}Y_{6i}Z_{6i}$ to $O_P - X_PY_PZ_P$ is as follows:

$$ {}^{O_P}T_{O_{6i}} = \begin{bmatrix} {}^{O_P}R_{O_{6i}} & {}^{O_P}O_{6i} \\ 0 & 1 \end{bmatrix} \tag{9} $$

In this formula, after the $O_P - X_PY_PZ_P$ system rotates in the specific order 3-2, it has the same posture as the $O_{6i} - X_{6i}Y_{6i}Z_{6i}$ system.

$$ {}^{O_P}R_{O_{6i}} = \begin{bmatrix} c\theta_{Z_P(i)} & -s\theta_{Z_P(i)} & 0 \\ s\theta_{Z_P(i)} & c\theta_{Z_P(i)} & 0 \\ 0 & 0 & 1 \end{bmatrix} \bullet \begin{bmatrix} c\theta_{Y'_P(i)} & 0 & s\theta_{Y'_P(i)} \\ 0 & 1 & 0 \\ -s\theta_{Y'_P(i)} & 0 & c\theta_{Y'_P(i)} \end{bmatrix} \tag{10} $$

Where: $\theta_{Z_P(i)} = \frac{\pi}{3}(i-3) - \frac{\theta_P}{2}$ $(i = 1, 3, 5)$, $\theta_{Z_P(i)} = \frac{\pi}{3}(i-4) + \frac{\theta_P}{2}$ $(i = 2, 4, 6)$, $\theta_{Y'_P(i)} = -\frac{\pi}{2}$.

Given the pose of the upper platform in the $O_B - X_BY_BZ_B$ system, ${}^{O_{0_i}}T_{O_{6i}}$ is determined using:

$$ {}^{O_{0_i}}T_{O_{6i}} = {}^{O_{0_i}}T_{O_B} \cdot {}^{O_B}T_{O_P} \cdot {}^{O_P}T_{O_{6i}} \tag{11} $$

To simplify the writing here, let:

$$ {}^{O_{0_i}}T_{O_{6i}} = \begin{bmatrix} n_x & o_x & a_x & p_x \\ n_y & o_y & a_y & p_y \\ n_z & o_z & a_z & p_z \\ 0 & 0 & 0 & 1 \end{bmatrix} \tag{12} $$

The Newton-Raphson iteration formula is constructed using ${}^{0}T_{6(i)} = {}^{O_{0_i}}T_{O_{6i}}$ to solve for the unknown D-H parameters in the kinematic chain of the i_{th} leg. The initial values of the variables must be given to enable solution of the nonlinear equations. The initial values $\theta_{1i}^{(0)}$, $\theta_{2i}^{(0)}$, $\theta_{3i}^{(0)}$, $L_{4i}^{(0)}$, $\theta_{5i}^{(0)}$, and $\theta_{6i}^{(0)}$ of θ_{1i}, θ_{2i}, θ_{3i}, L_{4i}, θ_{5i} and θ_{6i}, respectively, can be the variables at the zero position and are directly measured in 3 D model of the parallel platform.

$$ \begin{cases} f_{1i}(\theta_{1i}, \theta_{2i}, \theta_{3i}, L_{4i}, \theta_{5i}, \theta_{6i}) = {}^{0}T_{6(i)}(1,1) - {}^{O0i}\mathbf{T}0i_{O_{6i}}(1,1) = 0 \\ f_{2i}(\theta_{1i}, \theta_{2i}, \theta_{3i}, L_{4i}, \theta_{5i}, \theta_{6i}) = {}^{0}T_{6(i)}(2,1) - {}^{O0i}\mathbf{T}0i_{O_{6i}}(2,1) = 0 \\ \vdots \\ f_{12i}(\theta_{1i}, \theta_{2i}, \theta_{3i}, L_{4i}, \theta_{5i}, \theta_{6i}) = {}^{0}T_{6(i)}(3,4) - {}^{O0i}\mathbf{T}0i_{O_{6i}}(3,4) = 0 \end{cases} $$

$$ \begin{bmatrix} \theta_{1i} \\ \theta_{2i} \\ \theta_{3i} \\ L_{4i} \\ \theta_{5i} \\ \theta_{6i} \end{bmatrix}_{(n+1)} = \begin{bmatrix} \theta_{1i} \\ \theta_{2i} \\ \theta_{3i} \\ L_{4i} \\ \theta_{5i} \\ \theta_{6i} \end{bmatrix}_{(n)} - \begin{bmatrix} \frac{\partial f_{1i}}{\partial \theta_{1i}} & \frac{\partial f_{1i}}{\partial \theta_{2i}} & \frac{\partial f_{1i}}{\partial \theta_{3i}} & \frac{\partial f_{1i}}{\partial L_{4i}} & \frac{\partial f_{1i}}{\partial \theta_{5i}} & \frac{\partial f_{1i}}{\partial \theta_{6i}} \\ & & \vdots & & & \\ \frac{\partial f_{12i}}{\partial \theta_{1i}} & \frac{\partial f_{12i}}{\partial \theta_{2i}} & \frac{\partial f_{12i}}{\partial \theta_{3i}} & \frac{\partial f_{12i}}{\partial L_{4i}} & \frac{\partial f_{12i}}{\partial \theta_{5i}} & \frac{\partial f_{12i}}{\partial \theta_{6i}} \end{bmatrix}^{-1}_{(n)} \bullet \begin{bmatrix} f_{1i} \\ f_{2i} \\ \vdots \\ f_{12i} \end{bmatrix}_{(n)} \tag{13} $$

The iterative format shown in equation (13) can solve for the parameters in a manner that satisfies the error condition ($\pm 1 \times 10^{-10}$). The calculation flow for the inverse kinematics is shown in Figure 7.

Forward kinematics

The forward solution problem for the parallel platform is known as the displacement L_{4i} ($i = 1,\ldots,6$) required to solve for the pose P. There are no analytical solutions for nonlinear equations and it is difficult to solve them using the closed-loop vector method. Therefore, the problem is usually solved using numerical methods.

Given the displacements of the six legs, the equations that contain 30 unknown joint variables and six unknown pose variables for the mobile platform are established.

For a given leg displacement $L_G = [L_{1G}, L_{2G}, \ldots, L_{6G}]^T$, the function $F(P)$ is defined as follows: $F(P) = IKM(P) - L_G$ (14)

In the above formula, $IKM(P)$ is the inverse kinematics solution corresponding to pose P.

The Newton-Raphson numerical iteration method can be used to solve equation (14), and then the following solution is obtained:

$$P_{n+1} = P_n - \left(\frac{\partial F(P_n)}{\partial P}\right)^{-1} (IKM(P_n) - L_G) \tag{15}$$

In the above formula:

$$\frac{\partial F}{\partial p} = \begin{bmatrix} \frac{\partial L_1}{\partial X} & \frac{\partial L_1}{\partial Y} & \frac{\partial L_1}{\partial Z} & \frac{\partial L_1}{\partial \alpha} & \frac{\partial L_1}{\partial \beta} & \frac{\partial L_1}{\partial \gamma} \\ \vdots & \vdots & \vdots & \vdots & \vdots & \vdots \\ \frac{\partial L_6}{\partial X} & \frac{\partial L_6}{\partial Y} & \frac{\partial L_6}{\partial Z} & \frac{\partial L_6}{\partial \alpha} & \frac{\partial L_6}{\partial \beta} & \frac{\partial L_6}{\partial \gamma} \end{bmatrix} \tag{16}$$

Equation (16) is the Jacobi matrix between leg displacement and the posture of the upper platform. Given the initial value P_0, the numerical iteration is performed using the iteration scheme given in equation (15) until the rounding error reaches ($\pm 1 \times 10^{-9}$). It is better to choose the initial value at the ideal pose point or at a point on the simulation path.

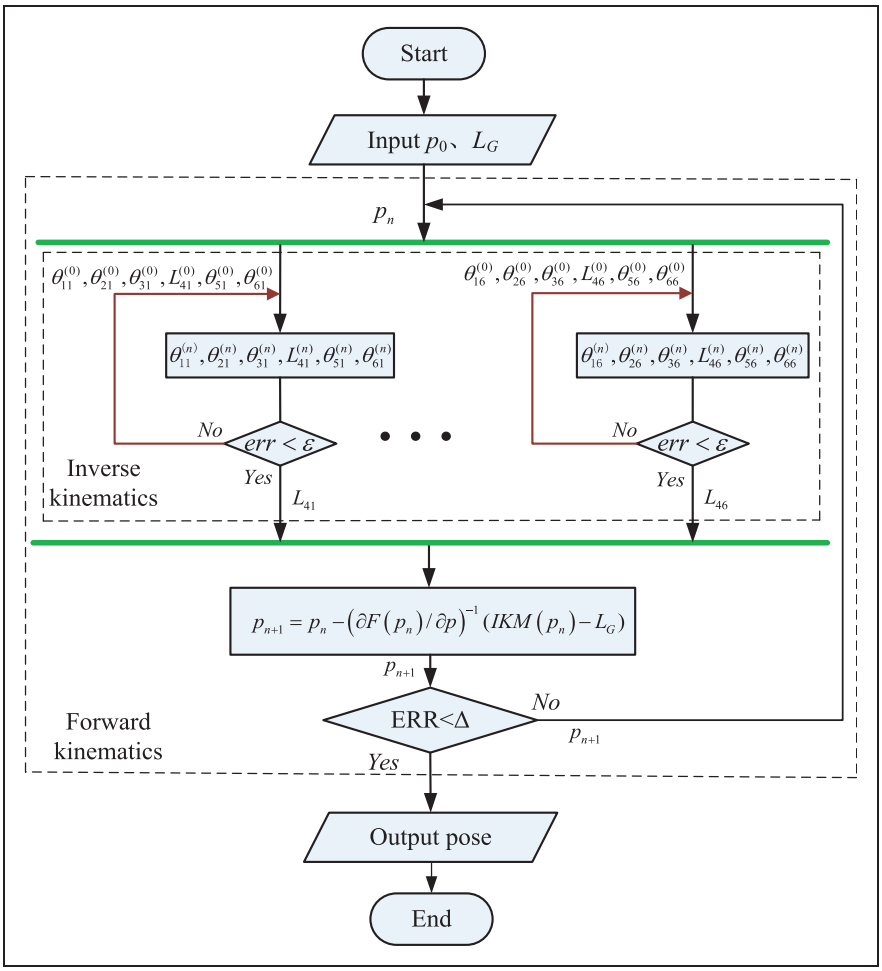

Figure 7. Solution procedure for forward kinematics problem.

The calculation flow for the forward kinematics is shown in Figure 7.

Kinematics simulation verification

Inverse kinematics simulation verification. To verify the correctness of the inverse kinematics modeling and the numerical iteration algorithm, the kinematics simulation is carried out using ADAMS software. Three reachable target poses are randomly selected, where P_1(1,2,353,3,3,3), P_2(0,0,348,−2,−1,4), P_3(5,−4,338, 0,0,0). The inverse kinematics solutions obtained using the iterative algorithm mentioned above (**I**) are compared to kinematic simulation results obtained using ADAMS(**S**), as shown in Table 3.

Table 3 shows that the results obtained using the numerical iteration algorithm are consistent with those obtained using ADAMS, and the maximum error is 0.063 pm. This error represents a combination of the control error of the iterative algorithm and the effective digital rounding error.

Forward kinematics simulation verification. First, L_{4i} ($i = 1, \ldots, 6$) for six target poses in ADAMS can be measured directly. The corresponding value of P can then be calculated using equation (15). Finally, the P value calculated using the algorithm is compared with the ADAMS input pose. The maximum position and posture error for the corresponding target poses is 0.755 pm and 6e-11° respectively.

Derivative movement caused by ball screw pair and its compensation

The rotating pair and the moving pair in the ball screw pair are coupled. This coupling produces a derivative motion that will then cause the pose errors of the parallel platform. The derivative motion expresses the relative rotation angle between the driving segment and the moving segment of the leg caused by passive spiral motion initiated by changes in the pose of the upper platform, thus resulting in leg length errors and pose errors. Therefore, it is necessary to compensate for the leg length error caused by the derivative motion.

According to the definition of the D-H parameters, the parameter θ_{3i} in the D-H parameters in Table 2, that is equal to the angle between the axis Z_{5i} and the axis Z_{2i}, represents the angle between the driving and moving segment of the leg, while $\Delta\theta_{3i}$ represents the relative rotation angle between the upper and lower leg, i.e., the derivative motion. Therefore, to compensate for the errors caused by the derivative motion, it is necessary to compensate for the rotation angle produced by the passive spiral motion to enable rotation angle control of the motor, as equation (17):

$$\Delta r_i = 2\pi \cdot \frac{\Delta L_i}{P} - \Delta\theta_{3i} \tag{17}$$

In the above: Δr_i– command angle of the i_{th} motor;
ΔL_i– displacement of the i_{th} leg in the target pose;
p– ball screw lead;
$\Delta\theta_{3i}$– rotation angle caused by the derivative motion.

By comparing the effects of compensation on the pose, the necessity for compensation is clarified. Two reachable poses are selected at random. P_i denotes the given pose, while P_i' and P_i'' denote the calculated pose without compensation and the corresponding pose with compensation from the ADAMS simulation, respectively, as shown in Table 4.

Table 4 shows that the maximum position error can reach 0.028 mm (28 μm) and the attitude error can reach 1.6″ without compensation. For parallel platforms that require micron-level accuracy, this error has a major impact on the adjustment accuracy of these platforms. The compensated pose is consistent with the given posture.

Inverse solution for speed and acceleration

Jacobi matrix of parallel platform

The pose of the upper platform is represented by the generalized coordinate vector $\mathbf{q} = [X_1, Y_1, Z_1,$

Table 3. Numerical iteration results and simulation results.

Leg displacement		L_1(mm)	L_2(mm)	L_3(mm)	L_4(mm)	L_5(mm)	L_6(mm)
P_1	**I**	0.298465 2360134	0.296776 3360603	0.302914 5784883	0.298068 3720075	0.289100 6079318	0.283446 0684061
P_1	**S**	0.298465 2360134	0.296776 3360603	0.302914 5784883	0.298068 3720074	0.289100 6079318	0.283446 0684061
P_2	**I**	0.290382 4083917	0.284005 6385122	0.290366 645316	0.286178 3338765	0.297299 9025448	0.291765 0810304
P_2	**S**	0.290382 4083917	0.284005 6385122	0.290366 645316	0.286178 3338765	0.297299 9025447	0.291765 0810304
P_3	**I**	0.278380 5065249	0.282361 7351791	0.281453 4897970	0.278933 6372831	0.281422 9233529	0.279961 62763070
P_3	**S**	0.278380 5065249	0.282361 7351790	0.281453 4897970	0.278933 6372831	0.281422 9233528	0.279961 62763070

Table 4. Comparison of pose values with or without compensation.

Pose	X (mm)	Y (mm)	Z (mm)	$\alpha(^\circ)$	$\beta(^\circ)$	$\gamma(^\circ)$
P_1	3.000000	–2.000000	–5.000000	1.000000	2.000000	3.000000
P_1'	3.006276	–1.988150	–4.980296	1.000350	1.999845	2.999555
P_1''	3.000000	–2.000000	–5.000000	1.000000	2.000000	3.000000
P_2	4.000000	3.000000	5.000000	–3.000000	1.000000	2.000000
P_2'	3.981227	3.005043	5.013016	–2.999753	1.000277	2.000410
P_2''	4.000000	3.000000	5.000000	–3.000000	1.000000	2.000000

$\varphi, \theta, \psi]^T$, while $\mathbf{t} = [X_1, Y_1, Z_1]^T$ represents the position of the origin of the upper platform-conjoined coordinate system and $\mathbf{q_t} = [\varphi, \theta, \psi]^T$ represents the upper platform's posture in the static coordinate system. Three elements in $\mathbf{q_t}$ represent Euler angles. The corresponding rotation transformation matrix is:

$$\mathrm{R} = Rot(z, \psi) \cdot Rot(y, \theta) \cdot Rot(x, \varphi) \tag{18}$$

Each leg kinematic chain in the parallel platform can be regarded as an RR-RP-RR series mechanism. Therefore, the kinematics theory for series mechanisms is used to analyze the leg, and the relationship between the velocity at the upper hinge point and the velocity of each joint in the leg is deduced.

In the i_{th} leg, the velocity equation relative to the previous coordinate system is:

$$^{O_{6i}}\mathbf{D} = {}^{O_{6i}}\mathbf{J} \cdot \mathbf{D}_\theta \tag{19}$$

Where: $^{O_{6i}}\mathbf{D}$ is the differential movement of the end of the leg relative to the $O_{6i} - X_{6i}Y_{6i}Z_{6i}$ system;

$^{O_{6i}}\mathbf{J}$ is the Jacobi matrix relative to the $O_{6i} - X_{6i}Y_{6i}Z_{6i}$ system;

$\mathbf{D}_\theta$ represents the differential motion of the six joints of the leg.

Equation (19) can then be rewritten as:

$$\begin{bmatrix} {}^{O_{6i}}d_x \\ {}^{O_{6i}}d_y \\ {}^{O_{6i}}d_z \\ {}^{O_{6i}}\delta_x \\ {}^{O_{6i}}\delta_y \\ {}^{O_{6i}}\delta_z \end{bmatrix} = \begin{bmatrix} {}^{O_{6i}}J_{11} & {}^{O_{6i}}J_{12} & \cdots & {}^{O_{6i}}J_{16} \\ {}^{O_{6i}}J_{21} & \cdots & & {}^{O_{6i}}J_{26} \\ & \vdots & & \\ {}^{O_{6i}}J_{61} & {}^{O_{6i}}J_{62} & \cdots & {}^{O_{6i}}J_{66} \end{bmatrix} \bullet \begin{bmatrix} d_{\theta_1} \\ d_{\theta_2} \\ d_{\theta_3} \\ d_{L_4} \\ d_{\theta_5} \\ d_{\theta_6} \end{bmatrix} \tag{20}$$

For the i_{th} leg of the parallel platform, if the combination of matrices $A_{1(i)}, A_{2(i)}, \ldots, A_{6(i)}$ is represented by the matrix **n**, **o**, **a**, **p**, then the elements of the four matrices above can be used to calculate $^{O_{6i}}\mathbf{J}$. The matrix **n**, **o**, **a**, **p** that corresponds to joints 1 to 6 is determined using the matrix $^{OB}T_{0i}\,{}^{0}T_{6(i)}$, $^{1}T_{6(i)}$, $^{2}T_{6(i)}$, $^{3}T_{6(i)}$, $^{4}T_{6(i)}$ and $^{5}T_{6(i)}$.

To obtain the Jacobi matrix for the parallel platform, it is first necessary to establish the relationship between the speed of the upper platform and the speeds of the six legs. When the pose **t** and the speed $\dot{\mathbf{q}}$ of $O_P - X_PY_PZ_P$ relative to $O_B - X_BY_BZ_B$ are given, then the speed of each joint in the legs can be obtained, where the fourth joint in each leg is a sliding joint. The relationship between the expansion speed $\dot{\mathbf{L}}$ of the six drive legs and the speed $\dot{\mathbf{q}}$ is then given as follows:

$$\dot{\mathbf{L}} = \begin{bmatrix} dL_{41}/dt \\ dL_{42}/dt \\ dL_{43}/dt \\ dL_{44}/dt \\ dL_{45}/dt \\ dL_{46}/dt \end{bmatrix} = \begin{bmatrix} {}^{O}\mathrm{J}_{4,\bullet}^{-1} \bullet {}^{O}\mathrm{D}/dt \\ {}^{O}\mathrm{J}_{4,\bullet}^{-1} \bullet {}^{O}\mathrm{D}/dt \\ {}^{O}\mathrm{J}_{4,\bullet}^{-1} \bullet {}^{O}\mathrm{D}/dt \\ {}^{O}\mathrm{J}_{4,\bullet}^{-1} \bullet {}^{O}\mathrm{D}/dt \\ {}^{O}\mathrm{J}_{4,\bullet}^{-1} \bullet {}^{O}\mathrm{D}/dt \\ {}^{O}\mathrm{J}_{4,\bullet}^{-1} \bullet {}^{O}\mathrm{D}/dt \end{bmatrix} = J\dot{q} \tag{21}$$

Where, $\dot{\mathrm{L}}$ is the matrix composed of the expansion speeds of the six driving legs;

J is the Jacobi matrix of the parallel platform.

J represents the conversion relationship between the speed $\dot{\mathbf{q}}$ relative to the $O_B - X_BY_BZ_B$ system and the expansion speed $\dot{\mathrm{L}}$ of the leg.

By calculating the time derivative of equation (21), the conversion formula between the acceleration $\ddot{\boldsymbol{q}}$ of $O_P - X_PY_PZ_P$ relative to $O_B - X_BY_BZ_B$ and the expansion acceleration $\ddot{\boldsymbol{L}}$ of the leg can be obtained as follows:

$$\ddot{\boldsymbol{L}} = \dot{\boldsymbol{J}}\dot{\boldsymbol{q}} + \boldsymbol{J}\ddot{\mathbf{q}} \tag{22}$$

Speed and acceleration analysis of the upper platform

Kinematics analysis mainly involves analysis of the speed and the acceleration of the upper platform in the static coordinate system and in the body coordinate system, and subsequently deducing the relationship between the speed, the acceleration and the generalized coordinates.

The generalized speed $\dot{\mathrm{q}}$ of the upper platform is given as follows:

$$\dot{\mathbf{q}} = \begin{bmatrix} \dot{\mathbf{t}}^{\boldsymbol{T}} & \omega^{\boldsymbol{T}} \end{bmatrix}^{\boldsymbol{T}} \tag{23}$$

In this formula, $\dot{\mathbf{t}}$ and ω represent the linear velocity vector and the angular velocity vector relative to the static coordinate system, respectively.

The following relationship exists between the angular velocity vector ω_P in the body coordinate system and the time derivative of $\mathbf{q_t}$:

$$\omega_p = \mathbf{E}\dot{\mathbf{q}}_t \tag{24}$$

In the above formula:

$$\mathbf{E} = \begin{bmatrix} 1 & 0 & -s\theta \\ 0 & c\varphi & s\varphi c\theta \\ 0 & -s\varphi & c\varphi c\theta \end{bmatrix}$$

The relationship between ω and ω_P is given as follows:

$$\omega = \mathbf{R}\omega_P \tag{25}$$

From equations (24) and (25), it is obtained:

$$\omega = \mathbf{RE}\dot{\mathbf{q}}_t \tag{26}$$

It can then be deduced that:

$$\dot{\mathbf{q}} = \begin{bmatrix} \dot{\mathbf{t}} \\ \omega \end{bmatrix} = \begin{bmatrix} \mathbf{I}_{3\times3} & \mathbf{0} \\ \mathbf{0} & \mathbf{RE} \end{bmatrix} \bullet \begin{bmatrix} \dot{\mathbf{t}} \\ \dot{\mathbf{q}}_t \end{bmatrix} = {}^{q}\mathbf{J}_{q_t} \begin{bmatrix} \dot{\mathbf{t}} \\ \dot{\mathbf{q}}_t \end{bmatrix} \tag{27}$$

${}^{q}\mathrm{J}_{q_t} = \begin{bmatrix} \mathrm{I}_{3\times3} & 0 \\ 0 & \mathrm{RE} \end{bmatrix}$ represents the Jacobi matrix of the time derivative of the generalized coordinate system for the generalized velocity of the upper platform.

$\dot{\boldsymbol{\omega}}_p$ is then obtained using equation (24):

$$\dot{\boldsymbol{\omega}}_p = \dot{\boldsymbol{E}}\dot{\boldsymbol{q}}_t + \boldsymbol{E}\ddot{\mathbf{q}}_t \tag{28}$$

After the time derivative of equation (25) is obtained, then it is obtained:

$$\dot{\boldsymbol{\omega}} = \dot{\boldsymbol{R}}\boldsymbol{\omega}_p + \boldsymbol{R}\dot{\omega}_p \tag{29}$$

$\dot{\boldsymbol{\omega}}$ is then obtained by entering $\dot{\mathbf{R}} = \boldsymbol{R}\tilde{\omega}_p$ into equation (29):

$$\dot{\boldsymbol{\omega}} = \boldsymbol{R}\tilde{\omega}_p\omega_p + \boldsymbol{R}\dot{\omega}_p = \boldsymbol{R}\dot{\omega}_p = \mathbf{R}(\dot{\boldsymbol{E}}\dot{\boldsymbol{q}}_t + \boldsymbol{E}\ddot{\mathbf{q}}_t) \tag{30}$$

The symbol "∼" in formula (30) represents an operator, which is defined as follows:

The skew symmetric matrix of vector $\mathbf{a} = [a_1, a_2, a_3]$ is denoted as $\tilde{\boldsymbol{a}}$, and its specific expression is as follows: $\tilde{\mathbf{a}} = \begin{bmatrix} 0 & -a_3 & a_2 \\ a_3 & 0 & -a_1 \\ -a_2 & a_1 & 0 \end{bmatrix}$

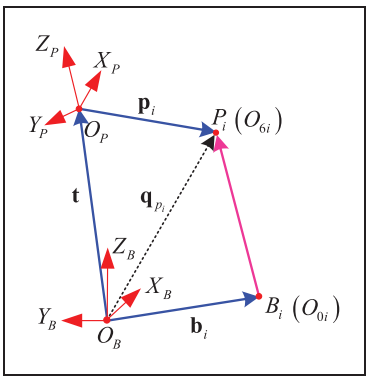

Figure 8. Vector diagram of the i_{th} leg.

Speed and acceleration analysis of upper hinge point

According to the vector relationship shown in Figure 8, the position vector for the upper hinge point $\mathbf{q}_{p_i}$ in the $O_B - X_B Y_B Z_B$ can be expressed as follows:

$$\mathbf{q}_{p_i} = \mathbf{t} + \mathbf{R}\mathbf{p}_i \tag{31}$$

Where, $\mathbf{t}$ is the position vector of O_P in the $O_B - X_B Y_B Z_B$ system;

$\mathbf{p}_i$ is the position vector of the upper hinge point p_i in the $O_P - X_P Y_P Z_P$ system.

The time derivative of equation (31) is calculated to give:

$$\dot{\mathbf{q}}_{p_i} = \dot{\mathbf{t}} + \dot{\boldsymbol{R}}\boldsymbol{p}_i = \dot{\mathbf{t}} + \dot{\boldsymbol{R}}\tilde{\omega}_p\mathbf{p}_i \tag{32}$$

Equation (32) is then obtained as follows:

$$\begin{aligned} \dot{\mathrm{q}}_{p_i} &= \dot{\mathrm{t}} + \tilde{\omega}\mathrm{R}\mathrm{p}_i = \dot{\mathrm{t}} + (\tilde{p}_{iB})^T\omega \\ &= \begin{bmatrix} \mathrm{I} & R\tilde{\mathrm{p}}_i^T\mathrm{R}^T \end{bmatrix} \bullet \begin{bmatrix} \dot{\mathrm{t}} \\ \omega \end{bmatrix} = {}^{qpi}\mathrm{J}p_{iq}\dot{\mathrm{q}} \end{aligned} \tag{33}$$

Where: ${}^{qpi}\mathrm{J}p_{iq}$ is the Jacobi matrix from the generalized speed of the upper platform to the speed of the upper hinge point, where ${}^{qpi}\mathrm{J}p_{iq} = \begin{bmatrix} \mathbf{I} & \boldsymbol{R}\tilde{\mathbf{p}}_i^T\mathbf{R}^T \end{bmatrix}$;

$\mathbf{p}_{iB}$ is the corresponding vector of vector $\boldsymbol{P}_i$ in the $\mathrm{O_B}$-$\mathrm{X_B Y_B Z_B}$ system.

The acceleration of the upper hinge point in the $O_B - X_B Y_B Z_B$ system is thus obtained as:

$$\ddot{q}_{p_i} = {}^{qpi}\mathrm{J}p_{iq}\ddot{q} + \tilde{\omega}^2\mathrm{R}\mathrm{p}_i \tag{34}$$

Testing

Resolution

To verify the actual performance of the platform, it is first necessary to test the prototype, as shown in

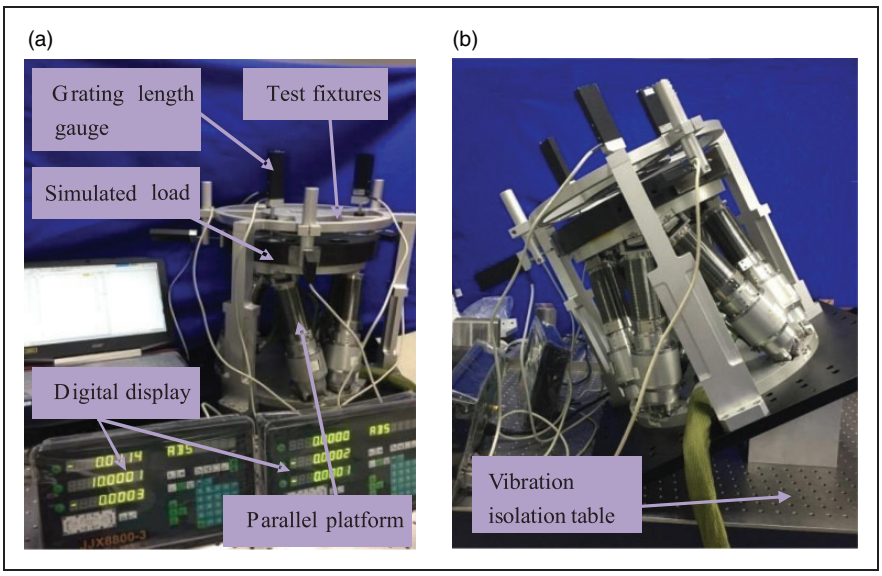

Figure 9. The test conditions: (a) Working condition 1, (b) Working condition 2.

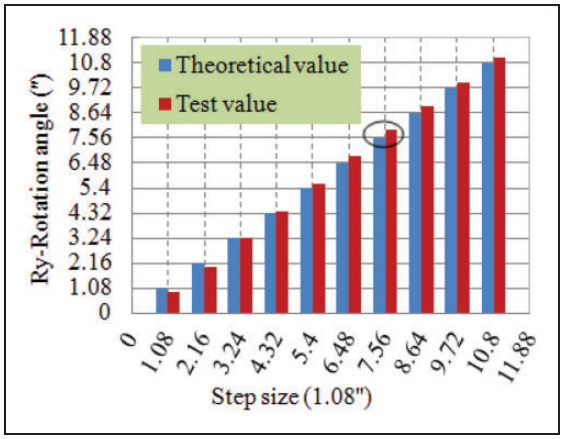

Figure 10. Resolution test in Ry direction.

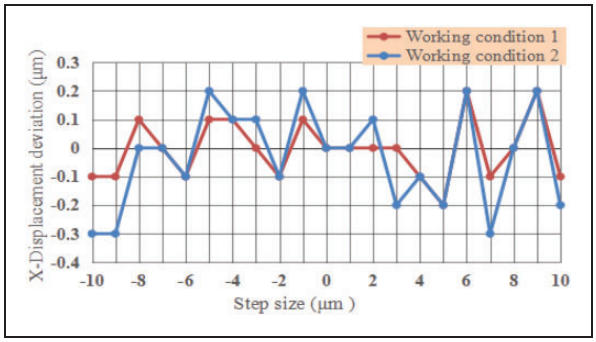

Figure 11. Resolution test in the X direction in the −10 to 10 μm range.

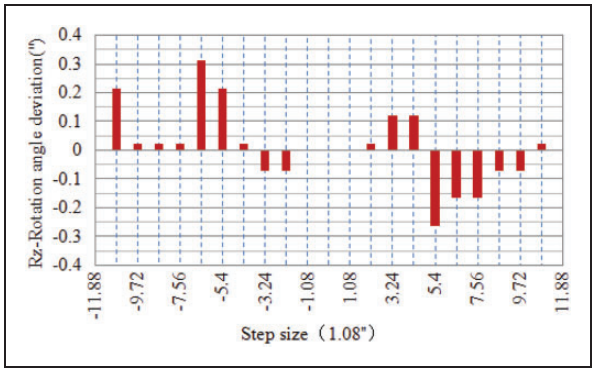

Figure 12. Resolution test in Rz direction in the −10.8″ to 10.8″ range.

Figure 9. The test conditions are as follows: the platform is placed horizontally on the vibration isolation table (working condition 1), and the platform is inclined at an angle of 30° (working condition 2), as shown in Figure 9(a) and (b), respectively. The translation resolution test uses a step size of 1 μm, while the rotation resolution test uses a step size of 1.08″ (0.0003°).

In working condition 1, the partial test results are as shown in Figures 10 and 11. These results show that the maximum deviations in the X and Ry directions are approximately 0.2 μm and 0.32″, respectively.

Under working condition 2, the partial test results are as shown in Figures 11 and 12

As the results show, the maximum deviations in the X and Rz direction are approximately 0.3 μm and 0.31″, respectively.

Under full stroke conditions, the resolution test results are based on the 3σ principle, and the statistical results are presented in Table 5.

Step accuracy

Measurement of the repetitive positioning accuracy is carried out using a fixed step length and multi-point cyclic measurements.

Under working condition 1, Figures 13 and 14 give the test curves in the X and Ry directions,

Table 5. Resolution test results.

Resolution test	Working condition 1	Working condition 2
X-Translation	1 μm ± 0.2 μm	1 μm ± 0.3 μm
Y-Translation	1 μm ± 0.2 μm	1 μm ± 0.2 μm
Z-Translation	1 μm ± 0.2 μm	1 μm ± 0.2 μm
X-Rotation	1.08″±0.36″	1.08″±0.3″
Y-Rotation	1.08″±0.32″	1.08″±0.3″
Z-Rotation	1.08″±0.43″	1.08″±031″

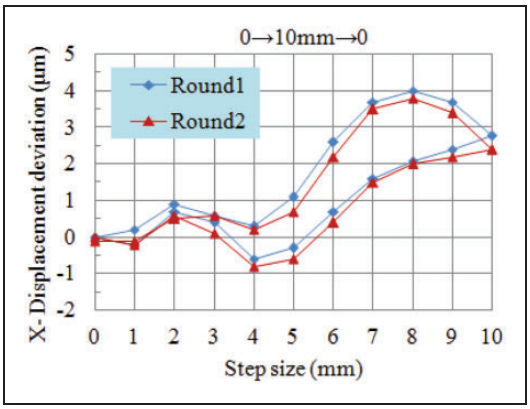

Figure 13. Repeated positioning accuracy testing in X direction.

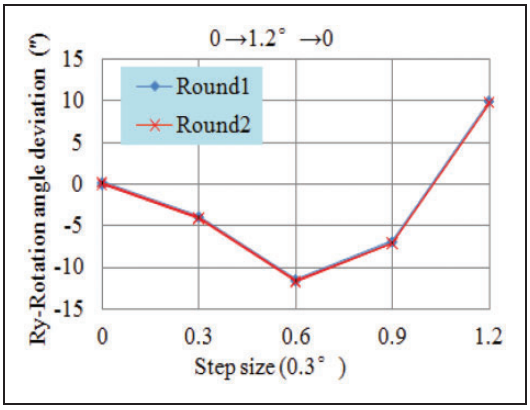

Figure 14. Repeated positioning accuracy testing in the Ry direction.

respectively. Under full stroke conditions, the repetitive positioning errors are X (±0.5 μm), Y (±0.5 μm), Z (±0.4 μm), Rx (±0.5″), Ry (±0.5″), and Rz (±0.4″).

Similarly, at full stroke of working condition 2, the repeat positioning errors are X ± 0.5 μm, Y ± 0.5 μm, Z ± 0.4 μm, Rx ±0.5″, Ry ±0.5″, and Rz ±0.4″.

Static stiffness

The static stiffness test mainly includes static stiffness testing of the legs and of the parallel platform. A static stiffness test of the legs is shown in Figure 15, and static stiffness testing of the platform is shown in Figures 16 and 17.

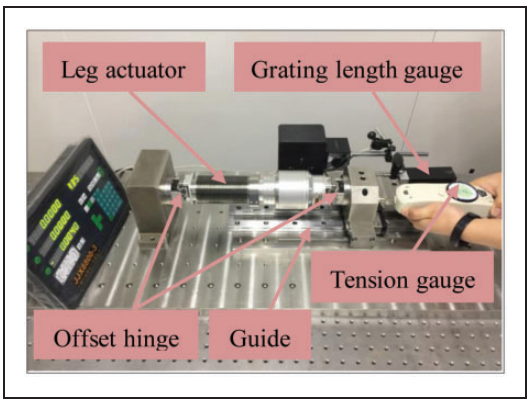

Figure 15. Static stiffness testing of legs.

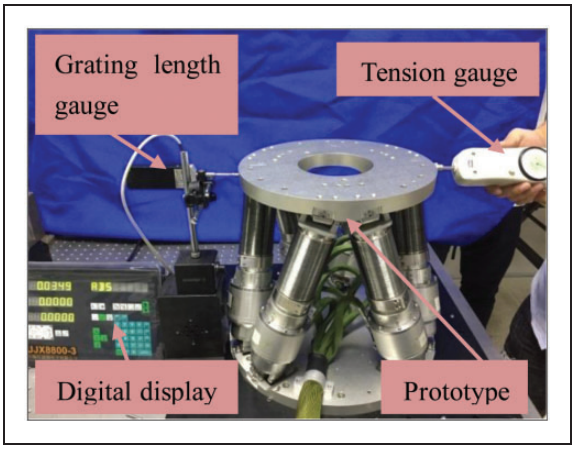

Figure 16. Horizontal static stiffness testing of the platform.

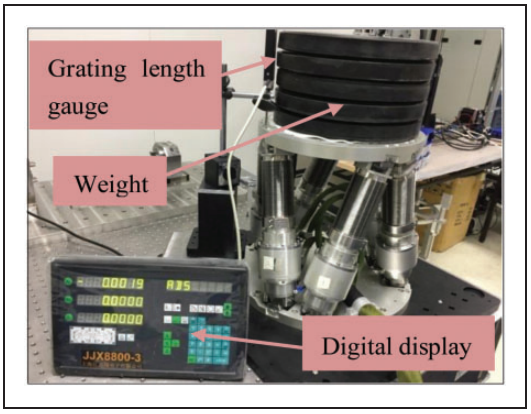

Figure 17. Axial static stiffness testing of the platform.

In Figure 18, both pull and pressure are applied to the legs and the static stiffness of the legs is measured to be 12.7 N/μm.

Three groups of tests are carried out in the axial static stiffness test, and the order in which the load is applied is: 0 N→300 N→0 N (step size of 50 N). Figure 19 shows that the Z-direction static stiffness of the platform is 125 N/μm. The lateral static stiffness of the platform is divided into the X-direction and Y-direction static stiffness values. The static

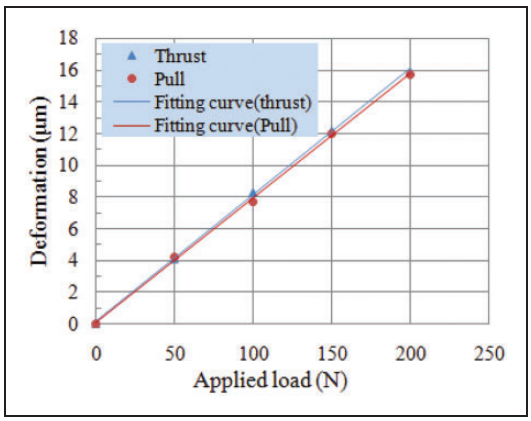

Figure 18. Axial static stiffness testing of the legs.

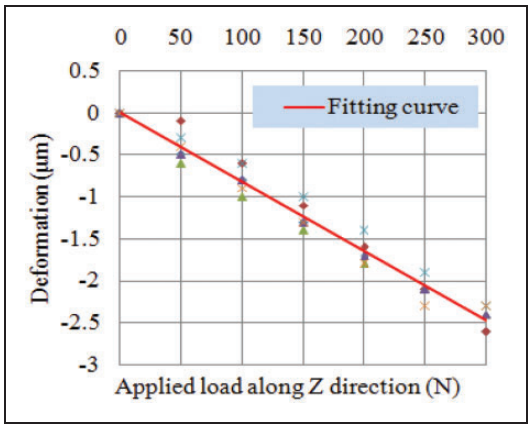

Figure 19. Z-direction static stiffness testing.

Table 6. Comparison of static stiffness of different positions.

	X-direction	Y-direction	Z-direction
P_0	2.985 N/μm	2.890 N/μm	125 N/μm
P_1	1.614N/μm	1.955N/μm	41.67N/μm
P_2	2.0683N/μm	2.306N/μm	71.43N/μm
P_3	1.97N/μm	2.38N/μm	66.67N/μm

stiffness in the X-direction is 2.985 N/μm, while the Y-direction static stiffness is 2.890 N/μm.

Three typical positions $P_1(0,0,30,0,0,4)$, $P_2(0,6,0,0,6,0)$, and $P_3(6,0,0,-6,0,0)$ are additionally selected, except zero position $P_0(0,0,0,0,0,0)$. The related static stiffness of the parallel platform is measured. The test results are shown in Table 6.

By comparing the static stiffness of the parallel platform in different positions, it is found that the static stiffness is significantly different, especially the axial stiffness changes greatly. With the change of position, the stiffness of each leg will change, resulting in the change in the stiffness of the parallel platform. This is of great enlightening significance to the subsequent research on the stiffness of the parallel platform, and the stiffness of the parallel platform needs further study.

Natural frequency testing

Fundamental frequency testing of the platform mainly includes axial and lateral fundamental frequency tests without a load (Figure 20(a)) and with a load (Figure 20(b)). The test system includes a vibration isolation table, a prototype, a computer, a hammer, and a spectrum analyzer. Firstly, the acceleration sensor is pasted on the moving platform, and the parallel platform is knocked with a hammer. The test system uploads the vibration response data

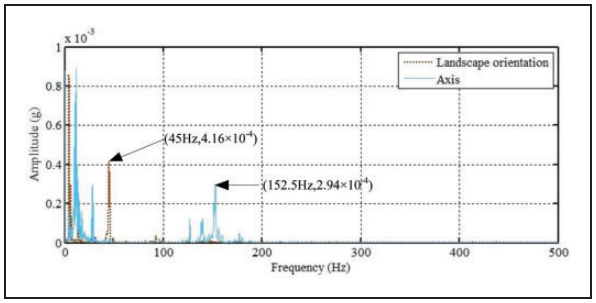

Figure 21. Vibrations response curve.

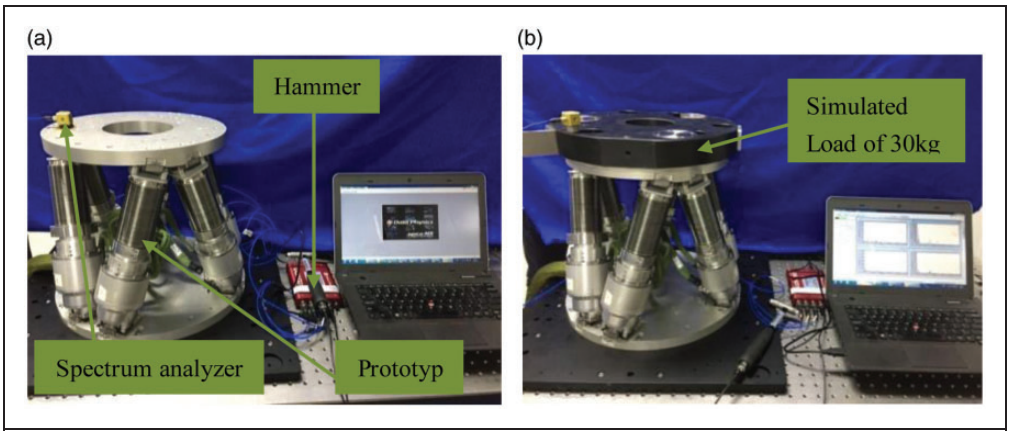

Figure 20. Fundamental frequency testing: (a) without load, (b) with load.

Table 7. Fundamental frequency test results.

Working condition	Without load	With load
Landscape orientation	94.06 Hz	45Hz
Axis	222.97 Hz	152.5 Hz

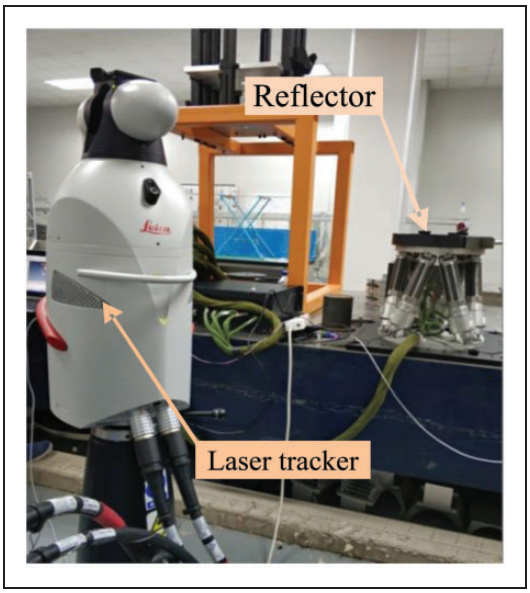

Figure 22. Stroke test.

Table 8. Parallel platform stroke test results.

Working condition	X	Y	Z	Rx	Ry	Rz
Stroke	±12mm	±12mm	±36mm	±6°	±6°	±8°

collected by the sensor to the spectrum analyzer, and generates the vibration response curve of the platform. Figure 21 is the vibration response curve of the platform with 30 kg load. The natural frequency corresponding to the low-frequency peak less than 30 Hz is the natural frequency of the vibration isolation platform where the test system is placed. The frequency at the two peaks indicated by the arrow respectively corresponds to the lateral and axial fundamental frequency of the whole platform. The test data are presented in Table 7.

Motion stroke test

The laser tracker is used to measure the strokes in the X, Y and Z translational directions and in the Rx, Ry and Rz rotational directions of the parallel platform. The stroke test is illustrated in Figure 22 and the results for the strokes are given in Table 8.

Conclusions

In this paper, a precise pointing adjustment mechanism for application to a large-aperture telescope submirror system is studied. To meet the precision, high stiffness and large working stroke requirements for the system, this paper proposes a 6-RR-RP-RR parallel platform with an RR offset hinge. The structure design of self-centering offset hinge with high rigidity and high precision is carried out. The two hinge axes of the offset hinge do not intersect, and the hinge offset variable is introduced, which makes its kinematics more complicated than that of the parallel mechanism using the universal hinge. It is difficult to solve effectively, and there is no analytical solution. Moreover, the existing methods have great limitations. This article innovatively introduces the D-H parameter method to solve the complex kinematics problem of the parallel mechanism, and a numerical iteration method is then used to solve the nonlinear equation. The parallel mechanism is regarded as a combination of series mechanism, therefore it can be decomposed into a series of series mechanisms for analysis, and then expand to the parallel mechanism. The D-H parameter method overcomes the shortcomings of the complex modeling process, large limitations and the poor continuity of the hinge motion constraint method. The D-H parameter method used in this paper has a simple modeling process, strong applicability and continuity, and can be widely applied to various parallel mechanisms, providing a new tool for the analysis and application of general parallel mechanisms. It provides an important, novel, and concise method for the kinematics problem of parallel mechanisms. Moreover, it can solve the variables of each joint, and facilitate the analysis of the velocity and acceleration of each joint, laying the foundation for the subsequent dynamic analysis. This paper has carried out a comprehensive test of the parallel platform to verify the performance, design index and the correctness of kinematic model of the platform from the experimental point of view. The results show that the platform provides excellent performance.

Declaration of Conflicting Interests

The author(s) declared no potential conflicts of interest with respect to the research, authorship, and/or publication of this article.

Funding

The author(s) disclosed receipt of the following financial support for the research, authorship, and/or publication of this article: this work was supported by the National Natural Science Foundation of China (grant number 11672290) and Jilin Scientific and Technological Development Program (20200404204YY).

ORCID iDs

Ha-si-ao-qi-er Han https://orcid.org/0000-0002-8427-3377
Chun-yang Han https://orcid.org/0000-0002-2509-1856

References

1. Shiga Y, Tanaka Y, Goto H, et al. Design of six degree-of-freedom tripod parallel mechanism for flight simulator. *Int J Automation Technol* 2011; 5: 715–721.
2. Yang JF, Xu ZB, Wu QW, et al. Dynamic modeling and control of a 6-DOF micro-vibration simulator. *Mech Mach Theory* 2016; 104: 350–369.
3. Gressler W, DeVries J, Hileman E, et al. LSST telescope and site status. *Proc. of SPIE 9145, Ground-based and airborne telescopes V*, Quebec, Canada, 22–27 June 2014, 91451A.
4. Kerr DR. Analysis, properties, and design of a stewart-platform transducer. *J Mech Transm Autom Des – Trans ASME* 1989; 111: 25–28.
5. Tian H, Li ZX, Meng L, et al. Conceptual design and dimensional synthesis of a novel 2-DOF translational parallel robot for pick-and-place operations. *J Mech Des* 2004; 126: 449–455.
6. Stepanenko O, Bonev IA and Zlatanov D. A new 4-DOF fully-parallel robot with decoupled rotation for Five-Axis micromachining applications. *J Mech Rob* 2019; 11: 031010.
7. Wang C, Fang Y and Guo S. Design and analysis of 3R2T and 3R3T parallel mechanisms with high rotational capability. *J Mech Rob* 2016; 8: 011004.
8. Xie FG, Liu XJ, Luo X, et al. Mobility, singularity, and kinematics analyses of a novel spatial parallel mechanism. *J Mech Rob* 2016; 8: 061022.
9. Narayanan MS, Kannan S, Zhou XB, et al. Parallel architecture manipulators for use in masticatory studies. *Int J Intell Mechatron Rob* 2011; 1: 100–122.
10. Terence E, Yang H, Juan SSA, et al. Kinematic optimization of a reconfigurable spherical parallel mechanism for robotic-assisted craniotomy. *J Mech Rob* 2019; 11: 060905.
11. Gómez PA, Mata V, Rodríguez MD, et al. Design and kinematic analysis of a novel 3UPS/RPU parallel kinematic mechanism with 2T2R motion for knee diagnosis and rehabilitation tasks. *J Mech Rob* 2017; 9: 061004.
12. Dalvand MM and Shirinzadeh B. Motion control analysis of parallel robot assisted minimally invasive surgery/microsurgery system (PRAMiSS). *Rob Computer-Integr Manuf* 2013; 29: 318–327.
13. Nakano T, Sugita N, Ueta T, et al. A parallel robot to assist vitreoretinal surgery. *Int J Comput Assist Radiol Surg* 2009; 4: 517–526.
14. Harib K and Srinivasan K. Kinematic and dynamic analysis of Stewart platform-based machine tool structures. *Robotica* 2003; 21: 541–554.
15. Kim JP and Ryu J. Inverse kinematic and dynamic analyses of 6-DOF PUS type parallel manipulators. *KSME Int J* 2002; 16: 13–23.
16. Song YM, Lian BB, Sun T, et al. A novel five-degree-of-freedom parallel manipulator and its kinematic optimization. *J Mech Rob* 2014; 6: 0410081–0410089.
17. Sun T, Yang SF, Huang T, et al. A generalized and analytical method to solve inverse kinematics of serial and parallel mechanisms using finite screw theory. In: *7th international workshop on computational kinematics,* Univ Poitiers, Fundamental & Appl Sci Fac, France, 22–24 May 2017.
18. Gan D, Liao Q, Dai JS, et al. Forward displacement analysis of a new 1CCC–5SPS parallel mechanism using Gröbner theory. *Proc IMechE, Part C: J Mechanical Engineering Science* 2009; 223: 1233–1241.
19. Liu GJ, Zheng ST, Ogbobe PO, et al. Inverse kinematic and dynamic analyses of the 6-UCU parallel manipulator. *Amm* 2011; 127: 172–180.
20. Großmann K and Kauschinger B. Eccentric universal joints for parallel kinematic machine tools: variants and kinematic transformations. *Prod Eng Res Devel* 2012; 6: 521–529.
21. Gloess R and Lula B. Challenges of extreme load hexapod design and modularization for large ground-based telescopes. *Proc SPIE Int Soc Opt Eng* 2010; 7739: 327–330.
22. Ji P and Wu HT. Kinematics analysis of an offset 3-UPU translational parallel robotic manipulator. *Rob Auton Syst* 2003; 42: 117–123.
23. Hu B and Lu Y. Analyses of kinematics, statics, and workspace of a 3-RRPRR parallel manipulator and its three isomeric mechanisms. *Proc IMechE, Part C: J Mechanical Engineering Science* 2008; 222: 1829–1837.
24. Dalvand MM and Shirinzadeh B. Forward kinematics analysis of offset 6-RRCRR parallel manipulators. *Proc IMechE, Part C: J Mechanical Engineering Science* 2011; 225: 3011–3018.
25. Shirinzadeh B and Dalvand MM. Kinematics analysis of 6-DOF parallel Micro-Manipulators with offset U-Joints: a case study. *Int J Intell Mechatron Rob* 2012; 2: 28–40.
26. Han H, Han CY, Xu ZB, et al. Kinematics analysis and testing of novel 6-P-RR-R-RR parallel platform with offset RR-joints. *Proc IMechE, Part C: J Mechanical Engineering Science* 2019; 233: 3512–3530.
27. Manocha D and Canny JF. Efficient inverse kinematics for general 6r manipulators. *IEEE Trans Robot Automat* 1994; 10: 648–657.
28. Fu Z, Yang W and Yang Z. Solution of inverse kinematics for 6R robot manipulators with offset wrist based on geometric algebra. *J Mech Rob* 2013; 5: 310081–310087.